Emission signal enhancement of laser ablation of metals (aluminum and titanium) by time delayed femtosecond double pulses from femtoseconds to nanoseconds

Jutta Mildner, Cristian Sarpe, Nadine Götte, Matthias Wollenhaupt, Thomas Baumert*

Institute of Physics and CINSaT, University of Kassel, Heinrich-Plett-Str. 40, D-34132 Kassel, Germany

ARTICLE INFO

ABSTRACT

Femtosecond double pulses with an inter pulse delay ranging from 100 fs up to 2 ns are used to study the dynamics of laser ablation of metals under ambient conditions far above the ablation threshold. To that end femtosecond double pulses of 30 fs pulse duration at 785 nm having the same intensities are focused onto the sample with a NA 0.5 microscope objective. Signals from element specific spectral line transitions and from reflection of the plasma plume are recorded as function of delay between the two pulses. The corresponding ablation structures are analyzed via atomic force microscopy. Based on these different observables four different enhancement regimes of the element specific signals are identified and discussed with respect to different transient stages of the ablation process. Both metals (Al and Ti) show qualitatively the same transient behavior. A maximum signal enhancement of about five is achieved at an inter pulse delay around 800 ps. The ablation volume is approximately the same as compared to the corresponding single pulse ablation volume with doubled fluence. This result serves as a route to increase the spatial resolution of far-field spectrochemical imaging via laser-induced breakdown spectroscopy on the few μm scale and below.

© 2013 Elsevier B.V. All rights reserved.

1. Introduction

Laser-induced breakdown spectroscopy (LIBS) is a well-established technique for spectrochemical element analysis in various applications [1–3]. Although LIBS does not achieve the sensitivity of other methods, as for example mass spectrometry, to date it offers a wide range of different advantages: No special sample preparation is needed and the analysis can be done in air under atmospheric conditions. As LIBS is a contactless method and only needs an optical access to the target the samples can be in any state of aggregation. Furthermore as laser radiation can be guided and focused over long distances it is possible to perform LIBS analyses at places that are difficult to access, e.g. in liquid fused metals or health hazardous environments. Due to these features LIBS is applied in many areas ranging from research to industry [4–6].

Usually nanosecond lasers are used in these applications. Femtosecond laser pulses on the other hand offer due to different ablation processes a more precise ablation with less thermal damage and with a higher reproducibility compared to nanosecond pulses [7–9]. Furthermore the femtosecond laser-induced plasma features a faster temporal decay and a reduced background, enabling to work at a higher repetition rate without any gate for data acquisition. On this basis femtosecond laser pulses are suitable to improve the spatial resolution and spectrochemical sensitivity in comparison to ns-LIBS [2,10,11] and facilitate fs-LIBS for biomedical applications [5,9,12], such as chemical mapping and depth profiling of complex biological systems [10]. For the same reasons, especially the fast processing speed, fs-LIBS is a promising tool for microanalysis of technical samples compared to well-established methods [6,13].

A high spatial resolution in LIBS can be achieved by tightly focusing the laser radiation onto the target (micro-LIBS) [6]. In the far-field and single-shot mode a resolution of 3 μm was demonstrated for 2D chemical mapping with nanosecond laser pulses [14] and (5-10) μm with femtosecond laser pulses respectively [15,16]. Single pulse ablation craters with diameters down to 450 nm were reported at the detection limit for fs-LIBS [17–19]. Recently we performed experiments for 2D mapping of lamellar structures in TiAl alloys with a spatial resolution of 2 μm by applying 10 consecutive shots per position to get a better signal to noise ratio [20]. The only way to further increase the spatial resolution and at the same time obtain spectrochemical information via LIBS to date is to work with near-field methods such as SNOM, resulting in crater diameters of 600 nm and larger [21–23].

* Corresponding author. Tel.: +49 561 804 4452; fax: +49 561 804 4453.
E-mail addresses: jmildner@uni-kassel.de (J. Mildner), tbaumert@uni-kassel.de (T. Baumert).

A promising approach to enhance the spectrochemical sensitivity for LIBS and to get a better understanding of the underlying physical processes is to apply double pulses. Double pulse LIBS in general can lead to an enhanced optical emission due to a more efficient energy deposition into the sample as well as into the plasma [24]. In the last years multiple investigations were done on double pulse laser ablation on a variety of sample systems, with different laser sources, pulse durations, geometric configurations and temporal separations between the two pulses, both in experiments and in simulations, see [24,25] and references therein. LIBS emission enhancement is strongly dependent on experimental parameters and sample systems. Most studies on femtosecond double pulse LIBS were done in vacuum resulting in emission enhancement ratios of 2–7 for maximal inter pulse delays ranging from 200 ps to 2 ns [26–29]. Emission enhancement in air was observed on Cu targets with factors of 6–11 at maximal achievable inter pulse delays of 110 ps and a fluence regime of 3–7 times the ablation threshold [30,31]. The dimensions of double pulse ablation structures are usually up to 50% smaller compared to single pulse ablation [30,32,33]. The resulting crater depths are smaller compared to single pulses of half the energy [33–35]. These experimental findings suggest double pulses for the enhancement of spatial resolution and spectrochemical sensitivity of fs-LIBS at the same time and motivate our study of the dynamics of laser ablation and plasma emission of metals in air on a wide range of inter pulse delays from 100 fs to 2 ns.

The choice of the samples is motivated by our work on chemical imaging of TiAl alloys [20], which are designed for structural components of aeronautics. Here we focus on pure metals to avoid a mixture of the individual alloying elements during ablation. Aluminum as a standard metal has been extensively studied in femtosecond laser ablation (see for example [36–45]) while comparatively less is reported on titanium (see for example [28,29,46–50]). The reason for aluminum being a popular sample system is that it features a free-electron-like electronic structure [51]. Titanium on the other hand is a transition metal with a considerably different and rather complex electronic structure: Its Fermi level lies in the center of a half filled d-band [51]. These differences in electronic structure have a considerable influence on the material parameters and possibly on the material's behavior during laser ablation and plasma emission. Studying both metals separately gives us the opportunity to check on these influences and their effect on the results of our fs-LIBS mapping technique used for analysis of metal alloys.

The paper is structured as follows: In Section 2 the experimental setup is presented. The samples are specified and detailed information is given on the data evaluation with special emphasis on the transient signals under study. In Sections 3.1 and 3.2, respectively, the experimental results are presented and discussed with respect to the physical processes taking place during laser ablation. Different subsections refer to the different enhancement regimes identified. These interpretations are then supported by structure analysis via atomic force microscopy (AFM) in Section 3.3. Section 3.4 completes our studies with an outlook for optimizing the spatial resolution and spectrochemical sensitivity.

2. Experiment

2.1. Experimental setup

Linearly polarized laser pulses with a pulse duration of 30 fs full width at half maximum (FWHM) and a central wavelength of 785 nm are provided at a repetition rate of 1 kHz by an amplified Ti:Sapphire laser system (*Femtolasers Femtopower Pro*). After passing a Mach-Zehnder interferometer (Fig. 1, right) the generated
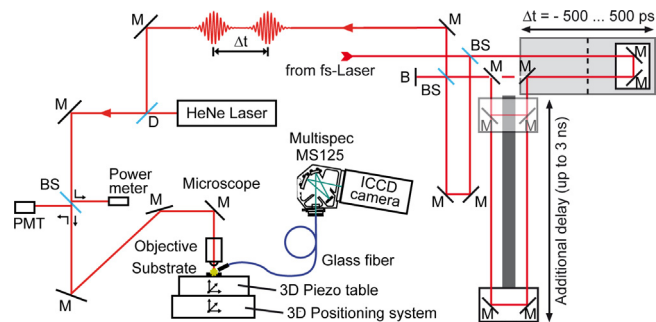

Fig. 1. Experimental setup for fs-LIBS (left) and schematics of a Mach-Zehnder interferometer with additional delay (right). A: attenuator; B: blocker; BS: beam splitter; D: dichroic; M: mirror; PMT: photomultiplier tube.

double pulses are guided to a modified microscope setup (Fig. 1, left) and focused onto the sample surface with a *Zeiss LD Epiplan* 50×/0.5 NA microscope objective. The lateral spot diameter was calculated to 1.4 μm at the $1/e^2$ value of intensity profile of the point-spread function [52]. The dispersion of the objective and remaining optical components in the beam path is precompensated by adjusting the prism compressor in the amplified laser system. In both beam lines of the interferometer neutral density filters are implemented to adjust the energy of both pulses separately. The total pulse energy in sum was set to 250 nJ and 350 nJ respectively, with an intensity ratio of 1:1.

The motorized translation stage of the interferometer has a travel range of 155 mm (*miCos HPS-170*) with feasible inter pulse delays up to 1 ns. To realize longer pulse delays up to 3 ns a second, manually controllable stage in form of a 50 cm rail is added to the delayed beam line. By varying the position of the slide on the manual rail, which is kept fixed during one measurement, it is possible to scan different delay ranges with the motorized stage. Successive delay ranges are chosen to overlap for reproducibility.

The sample is mounted on a 3-axis positioning system in air moving at constant speed to irradiate a fresh surface with each double pulse sequence, generating well-separated ablation structures. A tilt of the sample can be tracked with the 3-axis-system due to a confocal scan of its surface with a HeNe laser prior to the experiment. The laser-induced optical emission of the plasma plume is collected at an angle of 45° relative to the surface by a collimating quartz lens (NA 0.43) and guided through a UV-quartz glass fiber bundle to the spectrometer (*LOT-Oriel Multispec MS-125*). The grating of the spectrometer has 400 l/mm and is blazed at 400 nm. The generated spectra are recorded by an intensified CCD-camera (*Roper Scientific PIMAX*) at a repetition rate of 125 Hz with a shutter time of 50 ns and no camera delay. 250 spectra are acquired for each delay. The transient LIBS-signal is then determined by subtraction of a linearly interpolated background around a specific wavelength range of interest from its respective peak intensity (see Fig. 2). Analysis of the ablation structures is done via atomic force microscopy (AFM, *Bruker N8 NEOS*).

2.2. Sample system

Two different metal sample systems with high purity were studied in this paper: Aluminum (99.9%) and titanium (99.99%), being popular elements in various alloys for engineering applications, e.g. aircraft structural components. Detailed information on material parameters are given in Table 1. Averaged LIBS-spectra of each sample, Al and Ti respectively, are shown in Fig. 2. The spectra result from single pulse measurements with pulse energies of 250 nJ, averaged over 250 single-shot spectra. In the detected wavelength region of (230-750) nm the most prominent transition lines at 453 nm (Ti I) and 395 nm (Al I) were evaluated as well as a

Table 1
Sample specifications [54] and evaluated transitions [53] of studied metals.

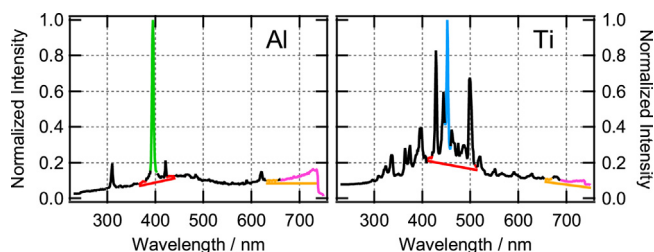| Material	Aluminum		Titanium	
CAS-No.	7429-90-5		7440-32-6	
Purity	99.9%		99.998%	
General properties	Metal		Transition metal	
Lattice structure	fcc		hcp	
Density	$2.70 \, \text{g/cm}^3$		$4.51 \, \text{g/cm}^3$	
Melting point	933.47 K		1943.15 K	
Boiling point	2792.15 K		3560.15 K	
Time for melting	1.9 ps [43]		2.0 ps [48]	
Electron–phonon coupling coefficient (300 K)	$2.45 \times 10^{17} \, \text{W/(Km}^3)$ [45]		$1.3 \times 10^{18} \, \text{W/(Km}^3)$ [51]	
Most prominent transitions [53]	Al I		Ti I	
	$3s^2 3p$	$3s^2 4s$	$3d^3(^4F)4s$	$3d^3(^4F)4p$
	394.401 nm	396.152 nm	453.324 nm	453.478 nm

Fig. 2. LIBS-spectra of aluminum (left) and titanium (right). All peaks except the purple ones are atomic transitions of Al and Ti, respectively. Only the most prominent transition lines are evaluated and highlighted in different colors: Al I 395 nm (green), Ti I 453 nm (blue), IR-signal 750 nm (purple). An interpolated background (red and yellow lines) is subtracted from the peak value of the corresponding spectral range. (For interpretation of the references to colour in this figure legend, the reader is referred to the web version of this article.)

third wavelength region around 700 nm, named IR-Signal. This signal originates from the lower wavelength end of the laser spectrum being reflected in the focal volume. It is getting more pronounced when the second laser pulse is reflected at the ablation plume created by the first pulse, which will be discussed in detail in Section 3. As the aluminum transition line at 309 nm showed the same temporal behavior as the doublet at 395 nm, second harmonic processes are not contributing to the transient signal. We therefore limit the presented results to the transition with higher emission intensity. Sample sizes were 10 mm in diameter and of 2 mm thickness. The surfaces are mechanically polished and cleaned with acetone prior to the experiment and again for 30 min in a super sonic bath just before AFM analyses were carried out.

3. Results and discussion

3.1. Experimental results

Double pulse experiments were performed on aluminum and titanium respectively. The applied pulse energies on both sample systems were 250 nJ in sum with equal intensity ratio between the two pulses. In the case of temporal symmetric scans for Al in Fig. 3(a) and (b), left, the total pulse energy was 350 nJ. These energies lie within the strong ablation regime [55]. They are about 20 times above the ablation threshold of 15 nJ for aluminum, corresponding to a mean fluence of $0.97 \, \text{J/cm}^2$ under our focusing conditions. For titanium it is even about 60 times above the threshold of 4 nJ equivalent to a mean fluence of $0.26 \, \text{J/cm}^2$. Both ablation thresholds result from single pulse experiments and evaluation via AFM scans following the evaluation methods suggested in [56,57]. Our threshold values are in good agreement with those determined in similar experiments by Li et al. and Mannion et al. $1.12 \, \text{J/cm}^2$ for Al [39] and $0.28 \, \text{J/cm}^2$ for Ti [49].

Two separate double pulse measurements were done on each sample system. In the first one the inter pulse delay was varied symmetrically on a logarithmic scale up to 500 ps and the second one on a longer delay range between 80 ps and 1080 ps in 50 ps-steps. In the case of Ti the longer delay range scaled up to 2080 ps. There were two reasons for this experimental approach: First to realize inter pulse delays longer than 1 ns an additive offset to the motorized translation stage had to be implemented (see Section 2.1). Secondly the symmetric scans have the advantage to make an immediate check on the quality and reliability of the data. Only if the obtained signals are symmetric in time, i.e. inter pulse delay, a proper beam adjustment of the interferometer is ensured and no beam drift or significant energy fluctuation occurred during the experiment. When no signal shift is observed within an overlapping delay range of more than 400 ps both scans can be regarded as one. Diverging scans are not considered.

As a reference single pulse experiments were done for the same total pulse energy keeping the delayed beam line blocked. By this procedure, the transient LIBS-signal can be normalized to its single pulse value obtaining the absolute enhancement ratio of the double pulse experiments given in Fig. 3 for Al on the left and for Ti on the right side. In addition, the corresponding reflected laser radiation of the second pulse from the interaction region (IR-signal) is shown on the right axes of Fig. 3(c) without normalization. In Fig. 3(b) the data points are connected by lines to guide the eye, whereas in graphs (a) and (c) phenomenological fits to the data were performed. For clarity, we omitted the standard deviation of the transient signals in the graphs. As an example the transient LIBS-signal at 800 ps inter pulse delay varies by 20% for aluminum and by 10% for titanium, see Fig. 3(c) left and right respectively. These values result from averaging the 250 evaluated single-shot signals at 395 nm and 453 nm respectively, before normalization. The standard deviation is typically larger for smaller signals, i.e. for smaller inter pulse delays. Note that these deviations cannot be applied when comparing enhancement factors or more precisely experimental results of separate double pulse measurements. Slightly different experimental conditions can lead to larger variations in the corresponding enhancement factors, see Fig. 3(a) and (b) for Al.

Both sample systems behave in a similar way: for inter pulse delays close to zero almost no signal dynamic is visible and the enhancement is negligible. At this stage the results resemble the behavior of single pulse experiments. After a few picoseconds pulse delay the LIBS-signal increases, reaching a maximum value around 800 ps with a total enhancement factor of 6 for Al and 2.5 for Ti, see Fig. 3(c) left and right respectively. For even longer delays the LIBS-signal starts to decrease again. Upon a closer look four different regimes of signal dynamics can be distinguished: (I) no signal dynamics below 1 ps; (II) at small pulse delays between 1 and 10 ps the signal is rising; (III) this signal increase saturates at intermediate delays around several ten ps; (IV) finally at longer pulse delays of more than 100 ps the signal rises again but with a smaller slope,
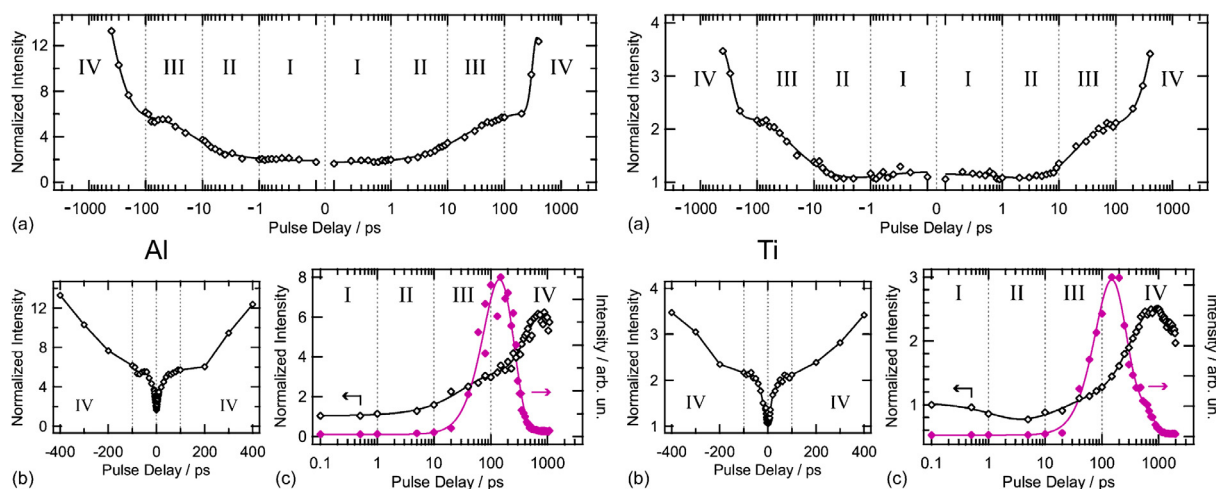
Fig. 3. Left: Transient DP-LIBS signal of aluminum on a logarithmic (a) and linear time scale (b) with a total pulse energy of 350 nJ and equal intensity ratio between the two pulses. (c) A different measurement done for 250 nJ and longer inter pulse delays (open squares, left axis) and corresponding IR-signal (filled squares, right axis): A maximum LIBS-signal enhancement is reached around (800 ± 30) ps; optimal reflection of the 2nd pulse is seen at approximately (150 ± 30) ps. Roman numerals label four different enhancement regimes: (I) no enhancement; (II) increase; (III) saturation behavior; (IV) further increase with maximum LIBS enhancement. Right: The same for titanium with a total pulse energy of 250 nJ in all three graphs (a), (b) and (c).

reaching its maximum at around (800 ± 30) ps for Al and Ti respectively. Note that in terms of absolute values the strongest increase is in regime IV, the second largest in regime III followed by regime II. The corresponding IR-signals on the contrary start to increase at later times (>10 ps) and assume their maximum values earlier around (150 ± 30) ps. Finally they approach the single pulse value at long inter pulse delays. The width of the IR-signal curve is much smaller compared to the transient LIBS-signal. The shapes of the transients presented here were reproduced many times and can be regarded as common.

3.2. Discussion

The different enhancement regimes of the transient LIBS-signal (I, II, III, IV) as well as the dynamics of the related IR-signal in these pump-probe experiments may be linked to different stages during ablation. In the following paragraphs these four regimes will be discussed in relation to the physical processes taking place on the studied time scales. We will focus our discussion on aluminum and only refer to titanium when differences become significant.

Regime I: Aluminum features a fast electron thermalization time well below 1 ps [42] and strong electron–phonon coupling [45]. The electron–phonon coupling coefficient of titanium is even one order of magnitude higher compared to aluminum [51]. During electron thermalization the second pulse has no major influence on the ablation mechanisms and the overall behavior resembles the case of single pulse ablation at the same total pulse energy (regime I). The second, delayed energy deposition into the system may only lead to a corresponding retarded electron–phonon coupling.

Regime II: After electron thermalization energy transfer to the lattice takes place due to electron–phonon coupling resulting in an equilibration of electron and lattice temperatures. When the lattice temperature exceeds the melting temperature of the material the system starts to melt. In the case of these large laser fluences homogeneous ultrafast melting is most likely to occur. According to reflectivity measurements of Kandyla et al. on Al and two-temperature calculations by Ye et al. on Ti the top surface layer of both metals melts within 2 ps after irradiation [43,48]. As the electron-lattice equilibration may not be completed within this time, especially for high fluences, there are continuing melt dynamics taking place. In this few ps regime the LIBS-signal starts to rise with increasing inter pulse delay (regime II).

Regime III: In the liquid phase the near dc electrical and electron heat conductivities of aluminum are smaller compared to the value of the solid [26,30,44]. The electrical conductivity by one order of magnitude [44], the heat conductivity by 73% [58]. Due to the reduced conductivities the absorbed energy of the second pulse is stronger localized in the sample (energy confinement) and cannot dissipate further into the bulk in lateral and axial direction. Therefore the liquid can reach much higher temperatures up to the region of an overcritical fluid. Additionally around 10% more energy can be absorbed by the metal as the reflectivity of metals is reduced in the liquid state [43,59]. The higher the temperature of the liquid phase, the higher the atomization degree of the plasma plume will be in the end [26] and therefore the LIBS-signal itself. The characteristic time for the electrical conductivity change is on the time scale for electron–phonon coupling, i.e. several ps. So the conductivity decreases at times when the LIBS-signal is rising continuously as well. This increase saturates several tens of picoseconds after heating (regime III). At this time the conductivity of liquid aluminum reaches its final value too. This correlates to the 40 ps timescale reported by [44] for Al. From this we conclude, that the first signal increase and the onset of the saturation behavior correlates with the melting of the sample due to the first pulse and overheating the resulting liquid with the second pulse.

On the time scales of our study the ablation plume behavior can be analyzed by the IR-signal dynamics representing the reflected laser radiation of the second pulse at the plasma plume created by the first pulse, see Fig. 3(c). The increasing IR-signal after approximately 20 ps inter pulse delay is a clear indication for plasma plume formation. At the onset of ablation a hot and dense plasma is created, which can efficiently shield the second laser pulse from the sample surface, as seen in double pulse ablation experiments of [33,34]. This also correlates with an almost constant LIBS-signal at the end of regime III and complements the saturation arguments given above. Note that according to density simulations on Al conducted by Colombier et al. ablation starts as well at 25 ps after irradiation with a 180 fs-pulse of 1 J/cm² fluence [36]. In this high fluence regime ablation will occur via critical point phase separation, i.e. atomization and fragmentation of the crystal. This ablation process was studied in detail via molecular dynamics simulations [40,60,61]. In this case ablation may start earlier compared to slower ablation processes at medium fluences, such as homogeneous nucleation and phase explosion.

Regime IV: The generated plasma plume will expand with time and separate from the surface with a speed of several km/s, as seen in time of flight measurements [50] and molecular dynamic simulations [41]. In the latter case a more directed evolution of the plume was found for higher fluences. This can be observed by the IR-signal dynamics as well: The reflection of the second pulse is getting more and more pronounced up to a maximum at 150 ps for Al and Ti respectively after irradiation by the first pulse. At this time the plasma plume may have the optimal state for reflection, i.e. pressure, density, temperature, size and/or position relative to the focus. With calculated plume expansion velocities of 6 km/s for Al [41] and measured ones of 7.5 km/s for Ti atoms [50] we estimate a plume position ≈1 μm above the sample surface. Although the cited velocities were determined under vacuum conditions, the plume propagation in air is similar to that observed in vacuum during the initial phase of expansion. This is valid as long as the mass of the ablation plume is higher compared to the mass of the displaced ambient gas [62]. Beyond this point the reflected signal is falling again due to ongoing plasma expansion. Maximal LIBS enhancement is observed at times when the IR-signal approaches its initial value. From this observation one can conclude that the plasma front becomes transparent and the second pulse can reach inner regions of the plume [27].

Various ways of interaction between the laser radiation and the plasma plume are possible at this point: (1) at these large fluences the laser radiation can be directly coupled into the present gas phase of neutral and ionized particles and inverse Bremsstrahlung absorption can heat the plasma [28]. (2) Amoruso *et al.* investigated in [37] the influence of different polarizations of two time-delayed laser pulses on the ion probe signal. If *p* polarized light was applied at inter pulse delays <500 ps the absorption was increased compared to *s* polarization. This was ascribed to resonance absorption in the plume, i.e. the interaction of the *p* polarized light wave with an overdense plasma, leading to an increased absorption compared to the usual collisional absorption by inverse Bremsstrahlung. As we focus our laser pulses at normal incidence onto the sample, this effect will not be relevant in our measurements. Further aspects of self-absorption can be studied using the experimental approach described in [63]. (3) Interaction of the second pulse with constituents of the plume may take place, such as disintegration of clusters, nanoparticles and larger liquid droplets as well as subsequent excitation of their resulting species. The latter is likely to contribute as our experimental conditions at short pulses and high fluences promote critical point phase separation, i.e. vaporization by atomization and fragmentation taking place at the same time during ablation. The result is a multi-component plume of atoms, ions, clusters and nanoparticles/droplets. According to molecular dynamics studies of Perez *et al.* the atoms and ions result from atomization while the clusters result from fragmentation [61]. Due to the drop of energy density within the sample ablation processes assigned to medium fluences, e.g. homogeneous nucleation and phase explosion, will occur as well, leading to the ejection of larger nanoparticles and droplets at later times. The amount of ejected droplets was calculated to be 15% of the total ejected mass in simulations conducted by Vidal *et al.* [40]. Grojo *et al.* identified two plume components of different velocities via *in situ* plasma diagnostics. The fast one corresponded to atoms and ions, whereas large particles corresponded to its slow component [50]. Due to this axial velocity distribution for the ejected material the large and heavy species may reach the optimal focus position at later times.

All these processes would lead to an enhancement of the transient LIBS-signal at long delays above 100 ps (regime IV). The LIBS-signal maximizes at an inter pulse delay of 800 ps for both metals and decreases again on an even longer time scale. The similar observations between the two sample systems are in agreement with further conclusions drawn by Grojo *et al.* They found the velocities of atoms and particles to be almost independent of the incident laser fluence as the thermalization of the electronic subsystem is completed before the energy transfer to the lattice takes place. In addition, the particle velocities were almost independent of the atomic mass of the different metals studied. The velocities of atoms on the contrary were 30% smaller for metals with doubled atomic masses [50]. Sonntag *et al.* obtained in molecular dynamics simulations a velocity distribution for Al clusters being independent of laser fluence as well [41].

3.3. AFM analysis

To support the conclusions drawn from transient signal dynamics in the previous section analyses of ablation structures were carried out via atomic force microscopy (AFM). AFM measurements were done regarding the inner diameter of the holes and their depth in non-contact mode. 10–20 structures of equal experimental conditions were scanned via AFM to obtain statistics. Evaluation of the AFM scans was done via scanning probe image processing software (*SPIP*, *Image Metrology*) to determine the structure dimensions. The reference structures created by single pulses of the same total pulse energy are evaluated the same way as the corresponding double pulse structures. The former are represented by red lines in Fig. 4. The standard deviation of each AFM scan was in the range of 10%. The dashed lines and accordingly the tinted backgrounds in Fig. 4 give the standard deviation of the single pulse values. Each measurement presented in this paper was conducted on a different day under slightly different experimental and analysis conditions resulting in slight differences for the absolute values for hole depth and diameter. The overall change in structure dimensions versus inter pulse delay was reproduced many times. Hence we focus our discussion only on trends for double pulse ablation in relation to single pulse ablation. To do so we again normalized the determined structure dimensions to their corresponding single pulse values at the same total pulse energy. For the applied single pulse energies of 250 and 350 nJ the inner diameters of aluminum holes, defined as the diameter within the melting rim at the level of the sample surface, were in the range of 2 μm. The crater depths and ablated volumes of aluminum were in the range of 400 nm and 0.7 μm³ respectively. Titanium dimensions were both slightly larger (about 10%) compared to aluminum. These values may vary by 30% on average, see Fig. 4(b).

The normalized AFM results for aluminum and titanium are given in Fig. 4 on the left and right side, respectively. They stem from exactly the same DP-LIBS measurements shown in Fig. 3. There is no such significant change visible compared to the strong increase in LIBS-signal. The structure's depth and diameter only change by 25–50% over the whole delay range. Particularly at 800 ps inter pulse delay the ablated volume reduces by 30% for Al and increases by 10% for Ti compared to single pulse values whereas the LIBS-signal is multiplied with a factor of 6 for Al and 2.5 for Ti. These factors can also be larger under slightly different experimental conditions, see Fig. 3(a). However the AFM results exhibit as well some dynamics: The inner diameters as well as the crater depths are comparable to the single pulse values for inter pulse delays below 1 ps (regime I). Between 1 and 10 ps (regime II) the dimensions decrease with increasing inter pulse delay. For the range of (10-100) ps (regime III) the values remain almost constant. On longer time scales >100 ps (regime IV) the holes become deeper, whereas the diameter stays constant or decreases slightly.

The dynamics of the individual structure dimensions, especially the ablation depth, resemble the processes discussed in the previous section: At small pulse delays (<1 ps, regime I) the holes are deep, i.e. on the order of the single pulse values. On these time scales the lattice is still cold and the electrons and ions do not interact yet. So only the total energy deposition into the electronic
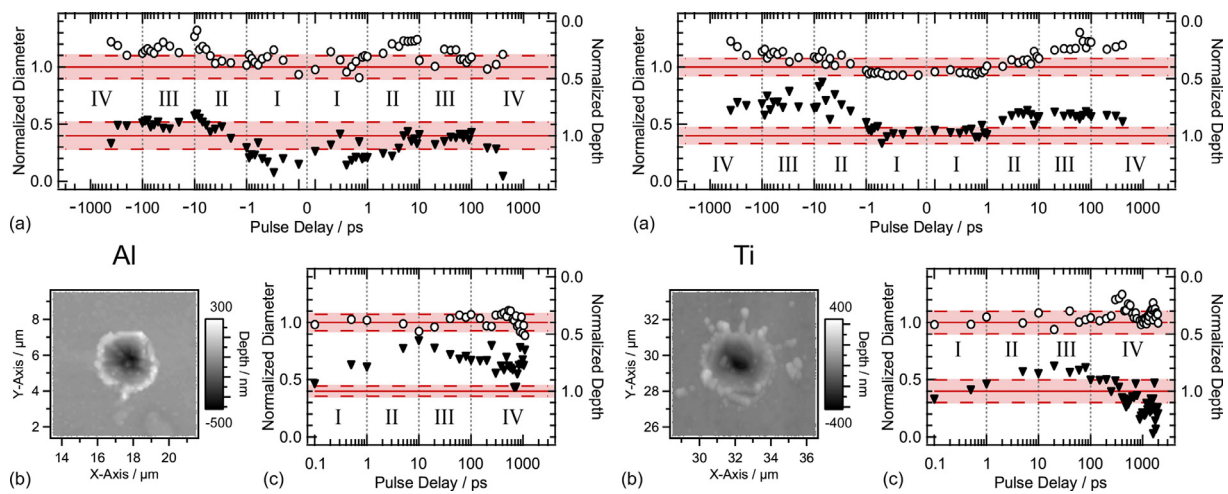
Fig. 4. Left: Inner diameter (open circles, left axis) and depth (filled triangles, right axis) of ablation structures in aluminum for a total pulse energy of 350 (a) and 250 nJ (c) from AFM scans. Both dimensions are normalized to their single pulse values (represented by red lines). The tinted background illustrates their standard deviation. The data in (a) and (c) result from structures of corresponding transients shown in Fig. 3 left. Roman numerals label again the different enhancement regimes introduced in Fig. 3. (b) AFM scan of a typical single pulse ablation structure in aluminum at 250 nJ. Right: The same for titanium with a total pulse energy of 250 nJ, compare Fig. 3 right. (For interpretation of the references to colour in this figure legend, the reader is referred to the web version of this article.)

subsystem is relevant for ablation. The resulting depth is then given by the penetration depth of the electrons [55]. Considering the high fluences applied ballistic penetration depths of the electrons may become relevant [64]. For inter pulse delays shorter than the time for electron–phonon coupling both pulses can therefore be regarded as one and the crater dimensions are the same for single pulses with doubled fluence.

The depth decrease between 1 and 10 ps (regime II) is in agreement with observations of [32–34]. This experimental finding can be correlated with an energy confinement of the second pulse in the sample, which was already discussed within the context of our transient LIBS-signal. The reduced conductivity in the liquid state may lead to a smaller extension of the melting region as the remaining solid phase is screened due to the energy confinement [65]. A different explanation could be the suppression of ablation caused by the second pulse. Povarnitsyn *et al.* conducted detailed hydrodynamic simulations of double pulse ablation in copper based on the two-temperature model [66,67] to explain the experimental results of [32]. They found a reduced ablation depth at inter pulse delays on the order of the electron–phonon relaxation time. In this regime the interaction of two different stress waves leads to a reduced ablation depth: The first laser pulse induces a pressure wave followed by a tensile wave, both propagating into the sample. A second, time delayed laser pulse results in a second pressure wave, which diminishes the tensile wave and therefore dumps the ablation process. This effect can only occur as long as both the tensile wave of the first pulse and the pressure wave of the second pulse propagate in the molten layer. As this mainly affects the spallation process, which only occurs at fluences near the threshold for ablation, we conclude the energy confinement to be the major effect for a reduced ablation depth in our experiments. In regime III (10 to 100 ps) no pronounced change in structure dimensions, especially regarding the depth, are observable. This may be due to plasma shielding discussed in Section 3.2.

Finally at longer pulse delays (>100 ps, regime IV) the holes are becoming deeper again. This coincides with the peak of the IR-signal and its following decrease. At the same time the LIBS-signal increases too. As discussed for the transients the plasma plume becomes transparent with expansion and more energy of the second pulse can reach the sample surface. Although the ablation rate is rising in this regime it only reaches the single pulse value again. The single pulse depth is only exceeded for titanium in Fig. 4(c),

right. This leads to the conclusion that a combination of two processes is the reason for the observed behavior: On the one hand a fraction of the second pulse is interacting with the plasma plume, while on the other hand an increasing part of the second pulse interacts with the sample more efficiently resulting in a higher LIBS-signal. The latter argument can be supplemented by the following: As the interaction of the vapor with the sample surface slows down the cooling rate, the surface remains liquid over a long time period of several ns up to μs. This ongoing heat transfer into the bulk leads to a larger contribution of heterogeneous melting to the overall melting depth, which becomes comparable to the dominating part of homogeneous melting observed in the spallation regime at low fluences [68]. This may result in deeper ablation craters than the ones created by single pulses of the same total pulse energy, as observed in titanium for longest inter pulse delays in Fig. 4(c), right. Also the slight increase in diameter, which is more apparent for Ti, may relate to the lateral expansion of the melting front by heterogeneous melting. This is a slow process with ~3% of the speed of sound, depending on the degree of overheating [69,70]. In addition, an interaction of the expanding ablation plume with the surface in terms of further ablation [30] and change in morphology [38] was discussed in the literature.

It is striking that the overall transient behavior is almost the same for the two different metals under study. In contrast the morphologies of aluminum and titanium ablation structures are quite different. Examples of typical single pulse ablation craters are given in Fig. 4(b), left and right respectively, in the form of AFM scans. Aluminum structures are smooth and round with a steep recast, whereas titanium structures are more cone-shaped and considerably splintered at the edges. The latter results from liquid droplets ejected during ablation.

3.4. Towards optimized parameters for fs-DP-LIBS

On the basis of our studies presented in the previous sections we proceeded to optimize the spatial resolution of fs-DP-LIBS. From our results in Section 3.1 we found the optimal inter pulse delay for signal enhancement to be around 800 ps for both metals under study. The corresponding LIBS-signal in Al at 800 ps was enhanced by a factor of 6 for 250 nJ total pulse energy. The ablated volumes being in the range of 0.5 μm³, which was 30% smaller compared to single pulses with double fluence. As discussed in Section 3.2
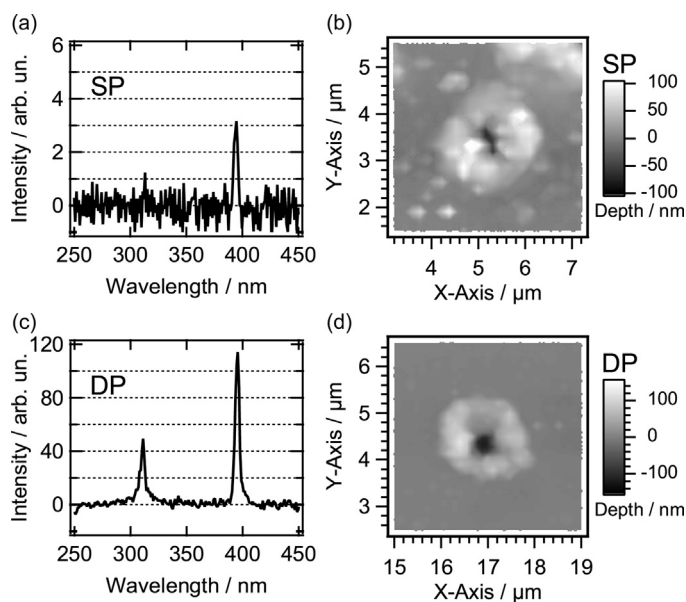
Fig. 5. Left column: Averaged LIBS-spectra of Al for a total pulse energy of 65 nJ obtained for single pulses (SP) (a) and double pulses (DP) with an inter pulse delay of 800 ps (c) respectively. Right column: AFM scans of the corresponding structures for single (b) and double pulse ablation (d). The Al transition at 395 nm is enhanced by a factor of about 40 whereas the inner diameters only increase from (450 ± 150) nm to (650 ± 150) nm.

the peak position of the transient LIBS-signal enhancement may be independent of incident laser fluence. We therefore conducted a measurement at 800 ps inter pulse delay with a significantly smaller pulse energy of 65 nJ, which is around 4 times above the threshold for ablation, see Section 3.1. The obtained LIBS-spectrum, averaged in this case over 600 single spectra, is shown in Fig. 5(c) with a standard deviation of 45% for signal maximum at 395 nm. The corresponding LIBS-spectrum obtained for single pulses with the same total pulse energy is shown in Fig. 5(a). The standard deviation in this case is about 650% due to the large noise of single pulse LIBS at low energies. A linearly interpolated background was subtracted in both graphs to account for the lower wavelength end of the laser spectrum being reflected in the focal volume, see Section 2.2. The comparison of both spectra clearly demonstrates that the Al transition at 395 nm is enhanced by a factor of about 40 and the noise is strongly reduced resulting in a much smaller standard deviation for single-shot DP-LIBS. AFM scans of the corresponding ablation structures are depicted in Fig. 5(b) and (d) respectively. The inner diameter for single pulse ablation at 65 nJ was in the range of (450 ± 150) nm, whereas the inner diameter for double pulses at 800 ps inter pulse delay was in the range of (650 ± 150) nm. The depth increased from (50 ± 30) nm to (100 ± 15) nm resulting in an ablated volume change by a factor of 3, i.e. from 4×10^{-3} μm^3 to 12×10^{-3} μm^3. Volumes were calculated with the help of the AFM software. These results serve as a route to increase the spatial resolution of far-field spectrochemical imaging via laser-induced breakdown spectroscopy in the few μm scale and even below.

4. Conclusions

In conclusion, pump-probe experiments on two different metals, aluminum and titanium, were carried out on a wide range of inter pulse delays. The experiments were performed with total pulse energies far above the ablation threshold and an intensity ratio of 1:1 between the two pulses. Both sample systems feature a similar behavior indicating that material dependent parameters have a minor influence on ultrashort pulse laser ablation in the high

fluence regime. Furthermore our experiments showed that double pulse LIBS in metals in general gives stronger LIBS-signals than single pulses at the same total pulse energy. Different enhancement regimes were identified and related to the physical processes taking place during ablation. Despite the fact that there is a change in ablation rate depending on the pulse separation time, we emphasize that (i) this change is rather small compared to the multiplied LIBS-signal and (ii) at times for optimal signal enhancement, i.e. 800 ps inter pulse delay, the structure dimensions are approximately the same as the corresponding single pulse values. As a consequence we were able to enhance the spectrochemical sensitivity of fs-LIBS while preserving the spatial resolution. Optimizing the spatial resolution on the Al sample by decreasing the total pulse energy, we obtained a more than one order of magnitude larger LIBS-signal with significantly smaller hole diameters down to (650 ± 150) nm. These results will serve to increase the spatial resolution of far-field LIBS for 2D spectrochemical analyses considerably [20]. In that publication the demonstrated resolution was about 2 μm. In the future the influence of different intensity ratios between the two pulses on the total enhancement factor and on the time dependent transient LIBS-signals will be investigated.

References

[1] J.D. Winefordner, I.B. Gornushkin, T. Correll, E. Gibb, B.W. Smith, N. Omenetto, Comparing several atomic spectroscopy methods to the super stars: special emphasis on laser induced breakdown spectrometry, LIBS, a future super star, J. Anal. At. Spectrom. 19 (2004) 1061–1083.

[2] E.L. Gurevich, R. Hergenröder, Femtosecond laser-induced breakdown spectroscopy: physics, applications, and perspectives, Appl. Spectrosc. 61 (2007) 233A–242A.

[3] A. Miziolek, V. Palleschi, I. Schechter, Laser-Induced Breakdown Spectroscopy (LIBS): Fundamentals and Applications, first ed., Cambridge University Press, New York, 2006.

[4] R. Gaudiuso, M. Dell'Aglio, O. De Pascale, G.S. Senesi, A. De Giacomo, Laser induced breakdown spectroscopy for elemental analysis in environmental, cultural heritage and space applications: a review of methods and results, Sensors (Basel) 10 (2010) 7434–7468.

[5] J. Kaiser, K. Novotny, M.Z. Martin, A. Hrdlicka, R. Malina, M. Hartl, V. Adam, R. Kizek, Trace elemental analysis by laser-induced breakdown spectroscopy – biological applications, Surf. Sci. Rep. 67 (2012) 233–243.

[6] V. Piñon, M.P. Mateo, G. Nicolas, Laser-induced breakdown spectroscopy for chemical mapping of materials, Appl. Spectros. Rev. 48 (2013) 357–383.

[7] J. Cheng, C.-S. Liu, S. Shang, D. Liu, W. Perrie, G. Dearden, K. Watkins, A review of ultrafast laser materials processing, Opt. Laser Technol. 46 (2013) 88–102.

[8] K. Sugioka, M. Meunier, A. Piqué, Laser Precision Microfabrication, first ed., Springer, Heidelberg, New York, 2010.

[9] F. Dausinger, F. Lichtner, H. Lubatschowski, Femtosecond Technology for Technical and Medical Applications, first ed., Springer, Berlin, Heidelberg, 2004.

[10] A. Assion, M. Wollenhaupt, L. Haag, F. Mayorov, C. Sarpe-Tudoran, M. Winter, U. Kutschera, T. Baumert, Femtosecond laser-induced-breakdown spectrometry for Ca^{2+} analysis of biological samples with high spatial resolution, Appl. Phys. B 77 (2003) 391–397.

[11] Y. Lu, V. Zorba, X. Mao, R. Zheng, R.E. Russo, UV fs–ns double-pulse laser induced breakdown spectroscopy for high spatial resolution chemical analysis, J. Anal. At. Spectrom. 28 (2013) 743–748.

[12] D. Santos Jr., L.C. Nunes, G.G.A. de Carvalho, M. da Silva Gomes, P.F. de Souza, F. de Oliveira Leme, L.G.C. dos Santos, F.J. Krug, Laser-induced breakdown spectroscopy for analysis of plant materials: a review, Spectrochim. Acta B 71–72 (2012) 3–13.

[13] H. Reingruber, H. Schröttner, A. Zankel, 3D elemental mapping in the ESEM. A combination of serial black-face SEM and EDS, Imag. Microscopy 2 (2011) 35–37.

[14] D. Menut, P. Fichet, J.L. Lacour, A. Rivoallan, P. Mauchien, Micro-laser-induced breakdown spectroscopy technique: a powerful method for performing quantitative surface mapping on conductive and nonconductive samples, Appl. Opt. 42 (2003) 6063–6071.

[15] H.M. Kuss, H. Mittelstadt, G. Muller, C. Nazikkol, Fast scanning laser-OES. I. Characterization of non-metallic inclusions in steel, Anal. Lett. 36 (2003) 659–665.

[16] I.V. Cravetchi, M.T. Taschuk, Y.Y. Tsui, R. Fedosejevs, Evaluation of femtosecond LIBS for spectrochemical microanalysis of aluminium alloys, Anal. Bioanal. Chem. 385 (2006) 287–294.

[17] V. Zorba, X. Mao, R.E. Russo, Ultrafast laser induced breakdown spectroscopy for high spatial resolution chemical analysis, Spectrochim. Acta B 66 (2011) 189–192.

[18] V. Zorba, X. Mao, R.E. Russo, Optical far- and near-field femtosecond laser ablation of Si for nanoscale chemical analysis, Anal. Bioanal. Chem. 396 (2010) 173–180.

[19] D.J. Hwang, H. Jeon, C.P. Grigoropoulos, J. Yoo, R.E. Russo, Femtosecond laser ablation induced plasma characteristics from submicron craters in thin metal films, Appl. Phys. Lett. 91 (2007) 251118-1–251118-3.

[20] W. Wessel, A. Brueckner-Foit, J. Mildner, L. Englert, L. Haag, A. Horn, M. Wollenhaupt, T. Baumert, Use of femtosecond laser-induced breakdown spectroscopy (fs-LIBS) for micro-crack analysis on the surface, Eng. Fract. Mech. 77 (2010) 1874–1883.

[21] O. Samek, A. Kurowski, S. Kittel, S. Kukhlevsky, R. Hergenröder, Ultra-short laser pulse ablation using shear-force feedback: femtosecond laser induced breakdown spectroscopy feasibility study, Spectrochim. Acta B 60 (2005) 1225–1229.

[22] D.J. Hwang, H. Jeon, C.P. Grigoropoulos, J. Yoo, R.E. Russo, Laser ablation-induced spectral plasma characteristics in optical far- and near-fields, J. Appl. Phys. 104 (2008) 013110-1–013110-12.

[23] D. Kossakovski, J.L. Beauchamp, Topographical and chemical microanalysis of surfaces with a scanning probe microscope and laser-induced breakdown spectroscopy, Anal. Chem. 72 (2000) 4731–4737.

[24] V.I. Babushok, F.C. DeLucia Jr., J.L. Gottfried, C.A. Munson, A.W. Miziolek, Double pulse laser ablation and plasma: laser induced breakdown spectroscopy signal enhancement, Spectrochim. Acta B 61 (2006) 999–1014.

[25] J. Scafffidi, S.M. Angel, D.A. Cremers, Emission enhancement mechanisms in dual-pulse LIBS, Anal. Chem. 78 (2006) 24–32.

[26] S. Noël, J. Hermann, Reducing nanoparticles in metal ablation plumes produced by two delayed short laser pulses, Appl. Phys. Lett. 94 (2009) 053120-1–053120-3.

[27] S. Amoruso, R. Bruzzese, X. Wang, Plume composition control in double pulse ultrafast laser ablation of metals, Appl. Phys. Lett. 95 (2009) 251501-1–251501-3.

[28] D. Scuderi, O. Albert, D. Moreau, P.P. Pronko, J. Etchepare, Interaction of a laser-produced plume with a second time delayed femtosecond pulse, Appl. Phys. Lett. 86 (2005) 071501-1–071501-3.

[29] E. Axente, I.N. Mihailescu, J. Herrmann, T.E. Itina, Probing electron–phonon coupling in metals via observations of ablation plumes produced by two delayed short laser pulses, Appl. Phys. Lett. 99 (2011) 081502-1–081502-3.

[30] S. Singha, Z. Hu, R.J. Gordon, Ablation and plasma emission produced by dual femtosecond laser pulses, J. Appl. Phys. 104 (2008) 113520-1–113520-10.

[31] J. Guo, T. Wang, J. Shao, T. Sun, R. Wang, A. Chen, Z. Hu, M. Jin, D. Ding, Emission enhancement ratio of the metal irradiated by femtosecond double-pulse laser, Opt. Commun. 285 (2012) 1895–1899.

[32] S. Noël, E. Axente, J. Hermann, Investigation of plumes produced by material ablation with two time-delayed femtosecond laser pulses, Appl. Surf. Sci. 255 (2009) 9738–9741.

[33] A. Semerok, C. Dutouquet, Ultrashort double pulse laser ablation of metals, Thin Solid Films 453–454 (2004) 501–505.

[34] T. Donnelly, J.G. Lunney, S. Amoruso, R. Bruzzese, X. Wang, X. Ni, Double pulse ultrafast laser ablation of nickel in vacuum, J. Appl. Phys. 106 (2009) 013304-1–013304-5.

[35] D.E. Roberts, A. du Plessis, L.R. Botha, Femtosecond laser ablation of silver foil with single and double pulses, Appl. Surf. Sci. 256 (2010) 1784–1792.

[36] J.P. Colombier, P. Combis, A. Rosenfeld, I.V. Hertel, E. Audouard, R. Stoian, Optimized energy coupling at ultrafast laser-irradiated metal surfaces by tailoring intensity envelopes: consequences for material removal from Al samples, Phys. Rev. B 74 (2006) 224106-1–224106-16.

[37] S. Amoruso, R. Bruzzese, X. Wang, J. Xia, Ultrafast laser ablation of metals with a pair of collinear laser pulses, Appl. Phys. Lett. 93 (2008) 191504-1–191504-3.

[38] N. Leng, L. Jiang, X. Li, C. Xu, P. Liu, Y. Lu, Femtosecond laser processing of fused silica and aluminum based on electron dynamics control by shaping pulse trains, Appl. Phys. A 109 (2012) 679–684.

[39] Q. Li, H. Lao, J. Lin, Y. Chen, X. Chen, Study of femtosecond ablation on aluminum film with 3D two-temperature model and experimental verifications, Appl. Phys. A 105 (2011) 125–129.

[40] F. Vidal, T.W. Johnston, S. Laville, O. Barthélemy, M. Chaker, B. Le Drogoff, J. Margot, M. Sabsabi, Critical-point phase separation in laser ablation of conductors, Phys. Rev. Lett. 86 (2001) 2573–2576.

[41] S. Sonntag, C. Trichet Paredes, J. Roth, H.-R. Trebin, Molecular dynamics simulations of cluster distribution from femtosecond laser ablation in aluminum, Appl. Phys. A 104 (2011) 559–565.

[42] B.Y. Mueller, B. Rethfeld, Relaxation dynamics in laser-excited metals under nonequilibrium conditions, Phys. Rev. B 87 (2013) 035139-1–035139-12.

[43] M. Kandyla, T. Shih, E. Mazur, Femtosecond dynamics of the laser-induced solid-to-liquid phase transition in aluminum, Phys. Rev. B 75 (2007) 214107.

[44] K.Y. Kim, B. Yellampalle, J.H. Glownia, A.J. Taylor, G. Rodriguez, Measurements of terahertz electrical conductivity of intense laser-heated dense aluminum plasmas, Phys. Rev. Lett. 100 (2008) 135002-1–135002-4.

[45] J.L. Hostetler, A.N. Smith, D.M. Czajkowsky, P.M. Norris, Measurement of the electron–phonon coupling factor dependence on film thickness and grain size in Au, Cr, and Al, Appl. Opt. 38 (1999) 3614–3620.

[46] A. De Giacomo, M. Dell'Aglio, A. Santagata, R. Teghil, Early stage emission spectroscopy study of metallic titanium plasma induced in air by femtosecond- and nanosecond-laser pulses, Spectrochim. Acta B 60 (2005) 935–947.

[47] A. Santagata, R. Teghil, A. De Giacomo, M. Dell'Aglio, G.P. Parisi, A. De Bonis, A. Galasso, Optical emission spectroscopy investigation of an ultra-short laser induced titanium plasma reheated by a ns laser pulse, Appl. Surf. Sci. 253 (2007) 7792–7797.

[48] M. Ye, C.P. Grigoropoulos, Time-of-flight and emission spectroscopy study of femtosecond laser ablation of titanium, J. Appl. Phys. 89 (2001) 5183–5190.

[49] P.T. Mannion, J. Magee, E. Coyne, G.M. O'Connor, T.J. Glynn, The effect of damage accumulation behaviour on ablation thresholds and damage morphology in ultrafast laser micro-machining of common metals in air, Appl. Surf. Sci. 233 (2004) 275–287.

[50] D. Grojo, J. Hermann, A. Perrone, Plasma analyses during femtosecond laser ablation of Ti, Zr, and Hf, J. Appl. Phys. 97 (2005) 063306-1–063306-9.

[51] Z. Lin, L.V. Zhigilei, V. Celli, Electron–phonon coupling and electron heat capacity of metals under conditions of strong electron–phonon nonequilibrium, Phys. Rev. B 77 (2008) 075133-1–075133-17.

[52] M. Martinez-Corral, Point spread function engineering in confocal scanning microscopy, Proc. SPIE 5182 (2003) 112–122.

[53] A. Kramida, Y. Ralchenko, J. Reader, NIST ASD Team, NIST Atomic Spectra Database (version 5.0), National Institute of Standards and Technology, Gaithersburg, MD, 2012, online available: http://physics.nist.gov/asd [19-Jun-2013].

[54] D.R. Lide, CRC Handbook of Chemistry and Physics, 86th ed., Taylor & Francis, Boca Raton, 2005.

[55] S. Nolte, C. Momma, H. Jacobs, A. Tünnermann, B.N. Chichkov, B. Wellegehausen, H. Welling, Ablation of metals by ultrashort laser pulses, J. Opt. Soc. Am. B 14 (1997) 2716–2722.

[56] J.M. Liu, Simple technique for measurements of pulsed Gaussian-beam spot sizes, Opt. Lett. 7 (1982) 196–198.

[57] B.N. Chichkov, C. Momma, S. Nolte, F. von Alvensleben, A. Tünnermann, Femtosecond, picosecond and nanosecond laser ablation of solids, Appl. Phys. A 63 (1996) 109–115.

[58] W.C. Kaye, T.H. Laby, Tables of Physical and Chemical Constants, 16th ed., Longman, Harlow, 1995.

[59] N. Semmar, M. Tebib, J. Tesar, N.N. Puscas, E. Amin-Chalhoub, Direct observation of phase transitions by time-resolved pyro/reflectometry of KrF laser-irradiated metal oxides and metals, Appl. Surf. Sci. 255 (2009) 5549–5552.

[60] C. Cheng, X. Xu, Mechanisms of decomposition of metal during femtosecond laser ablation, Phys. Rev. B 72 (2005) 165415-1–165415-15.

[61] D. Perez, L.J. Lewis, Molecular-dynamics study of ablation of solids under femtosecond laser pulses, Phys. Rev. B 67 (2003) 184102-1–184102-15.

[62] N. Arnold, J. Gruber, J. Heitz, Spherical expansion of the vapor plume into ambient gas: an analytical model, Appl. Phys. A 69 (1999) S87–S93.

[63] H.-Y. Moon, K.K. Herrera, N. Omenetto, B.W. Smith, J.D. Winefordner, On the usefulness of a duplicating mirror to evaluate self-absorption effects in laser induced breakdown spectroscopy, Spectrochim. Acta B 64 (2009) 702–713.

[64] J. Byskov-Nielsen, J.-M. Savolainen, M.S. Christensen, P. Balling, Ultra-short pulse laser ablation of copper, silver and tungsten: experimental data and two-temperature model simulations, Appl. Phys. A 103 (2011) 447–453.

[65] M. Guillermin, A. Klini, J.P. Colombier, F. Garrelie, D. Gray, C. Liebig, E. Audouard, C. Fotakis, R. Stoian, Tuning spectral properties of ultrafast laser ablation plasmas from brass using adaptive temporal pulse shaping, Opt. Express 18 (2010) 11159–11172.

[66] M.E. Povarnitsyn, T.E. Itina, K.V. Khishchenko, P.R. Levashov, Suppression of ablation in femtosecond double-pulse experiments, Phys. Rev. Lett. 103 (2009) 195002-1–195002-4.

[67] M.E. Povarnitsyn, T.E. Itina, P.R. Levashov, K.V. Khishchenko, Simulation of ultrashort double-pulse laser ablation, Appl. Surf. Sci. 257 (2011) 5168–5171.

[68] L.V. Zhigilei, Z. Lin, D.S. Ivanov, Atomistic modeling of short pulse laser ablation of metals: connections between melting, spallation, and phase explosion, J. Phys. Chem. C 113 (2009) 11892–11906.

[69] L.V. Zhigilei, Z. Lin, D.S. Ivanov, E. Leveugle, W.H. Duff, D. Thomas, C. Sevilla, S.J. Guy, Atomic/molecular-level simulations of laser-materials interactions, in: A. Miotello, P.M. Ossi (Eds.), Laser-Surface Interactions for New Materials Production: Tailoring Structure and Properties, Springer Series in Materials Science 130, Springer, New York, 2010, pp. 43–79.

[70] L.V. Zhigilei, D.S. Ivanov, E. Leveugle, B. Sadigh, E.M. Bringa, Computer modeling of laser melting and spallation of metal targets, Proc. SPIE 5448 (2004) 505–519.